

Deep convolutional neural networks for segmenting 3D *in vivo* multiphoton images of vasculature in Alzheimer disease mouse models

Mohammad Haft-Javaherian^a, Linjing Fang^a, Victorine Muse^a, Chris B. Schaffer^a, Nozomi Nishimura^a, Mert R. Sabuncu^{a,b,*}

^a*Nancy E. and Peter C. Meinig School of Biomedical Engineering, Cornell University, Ithaca, NY, USA*

^b*School of Electrical and Computer Engineering, Cornell University, Ithaca, NY, USA*

Abstract

The health and function of tissue rely on its vasculature network to provide reliable blood perfusion. Volumetric imaging approaches, such as multiphoton microscopy, are able to generate detailed 3D images of blood vessels that could contribute to our understanding of the role of vascular structure in normal physiology and in disease mechanisms. The segmentation of vessels, a core image analysis problem, is a bottleneck that has prevented the systematic comparison of 3D vascular architecture across experimental populations. We explored the use of convolutional neural networks to segment 3D vessels within volumetric *in vivo* images acquired by multiphoton microscopy. We evaluated different network architectures and machine learning techniques in the context of this segmentation problem. We show that our optimized convolutional neural network architecture, which we call *DeepVess*, yielded a segmentation accuracy that was better than both the current state-of-the-art and a trained human annotator, while also being orders of magnitude faster. To explore the effects of aging and Alzheimer’s disease on capillaries, we applied *DeepVess* to 3D images of cortical blood vessels in young and old mouse models of Alzheimer’s disease and wild type littermates. We found little difference in the distribution of capil-

*Corresponding author

Email address: msabuncu@cornell.edu (Mert R. Sabuncu)

lary diameter or tortuosity between these groups, but did note a decrease in the number of longer capillary segments ($> 75\mu m$) in aged animals as compared to young, in both wild type and Alzheimer’s disease mouse models.

Keywords: Vessel segmentation, Vascular segmentation, *In vivo* multiphoton microscopy, Convolutional neural network, Deep neural network, Centerline extraction, Aging, Alzheimer’s disease

Highlights.

- A convolutional neural network, *DeepVess*, successfully segmented vasculature structure from 3D image stacks acquired *in vivo*.
- *DeepVess* outperformed a trained human annotator and current state-of-the-art algorithms in segmentation accuracy.
- Measured capillary diameter, length, and tortuosity, based on large data sets across multiple animals, for young and old mice in both wild type and Alzheimers disease models.

1. Introduction

The performance of organs and tissues depend critically on the delivery of nutrients and removal of metabolic products by the vasculature. Blood flow deficits due to disease related factors or aging often leads to functional impairment [1]. In particular, the brain has essentially no energy reserve and relies on the vasculature to provide uninterrupted blood perfusion [2].

Multiple image modalities can be used to study vascular structure and dynamics, each offering tradeoffs between the smallest vessels that can be resolved and the volume of tissue that can be imaged. Recent work with several modalities, including photoacoustic microscopy [3], optical coherence tomography [4], and multiphoton microscopy (MPM) [5], enable individual capillaries to be resolved in 3D over volumes approaching $1mm^3$ in living animals. The analysis of such images is one of the most critical and time-consuming tasks of this research, especially when it has to be done manually.

For example, in our own work we investigated the mechanisms leading to reduced brain blood flow in mouse models of Alzheimers disease (AD), which required extracting topology from capillary networks each with $\sim 1,000$ vessels from dozens of animals. The manual tracing of these networks required $\sim 40\times$ the time required to acquire the images, greatly slowing research progress [6]. The labor involved in such tasks limits our ability to investigate the vital link between capillary function and many different diseases.

In this paper, we consider the segmentation of vessels, a core image analysis problem that has received considerable attention [7, 8]. As in other segmentation and computer vision problems, in recent years deep neural networks (DNNs) have offered state-of-the-art performance [9]. DNN approaches often rely on formulating the problem as supervised classification (or regression), where a neural network model is trained on some (manually) labeled data. For a survey on deep learning in medical image analysis, see a recent review by Litjens et al. [9].

Here, we explore the use of a convolutional neural network (CNN) to segment 3D vessels within volumetric *in vivo* MPM images. We conduct a thorough study of different network architectures and machine learning techniques in the context of our segmentation problem. We apply the final model, which we call *DeepVess*, on image stacks of cortical blood vessels in mouse models of AD and wild type littermates. Our experimental results show that *DeepVess* yields segmentation accuracy that is better than current state-of-the-art and a trained human annotator, while being orders of magnitude faster.

2. Related work

Blood vessel segmentation is one of the most common and time-consuming tasks in biomedical image analysis. This problem can either be approached in 2D or 3D, depending on the specifics of the application and analytic technique. The most established blood vessel segmentation methods are developed for 2D retinography [10] and 3D CT/MRI [8].

Among segmentation methods, region-based methods are well-known for their simplicity and low computational cost [11]. For example, Yi and Ra [12] developed a 3D region growing vessel segmentation method based on local cube tracking. In related work, Mille and Cohen [13] used a 3D parametric deformable model based on the explicit representation of a vessel tree to generate center-lines. In recent years, these traditional segmentation methods have become less popular and are considered to be limited in comparison to deep learning methods, because they require handcrafted filters, features, or logical rules and often yield lower accuracy.

Today, in problems that are closely related to ours, various deep learning techniques dominate state-of-the-art. For instance, in a recent Kaggle challenge for diabetic retinopathy detection within color fundus images, deep learning was used by most of the 661 participant teams, including the top four teams. Interestingly, those top four methods surpassed the average human accuracy. Subsequently, Gulshan et al. [14] adopted the Google Inception V3 network [15] for this task and reached the accuracy of seven ophthalmologists combined. For retinal blood vessel segmentation, Wu et al. [16] used a CNN-based approach to extract the entire connected vessel tree. Fu et al. [17] proposed to add a conditional random fields (CRF) to post-process the CNN segmentation output. They further improved their method by replacing the CRF with a recurrent neural network (RNN), which allows them to train the complete network in an end-to-end fashion [18]. Further, Maninis et al. [19] addressed retinal vessel and optic disc segmentation problems using one CNN network and could surpass the human expert.

There are 3D capillary image datasets in mice [11] and human [20] that were segmented using traditional segmentation methods and have illustrated the scientific value of such information, but few such datasets are available. To the best of our knowledge, there are only two studies that used deep learning for our problem: vascular image analysis of multi-photon microscopy (MPM) images. Teikari et al. [21] proposed a hybrid 2D-3D CNN architecture to produce state-of-the-art vessel segmentation results in 3D microscopy images. The limitations

of their method include the use of 2D convolutions and 2D CRFs, which restrict the full exploitation of the information along the third dimension. In addition, they trained their network based on static *in vitro* images rather than *in vivo* images. Segmentation of *in vitro* images is often less challenging as they do not include motion artifacts. The other study was conducted by Bates et al. [22], where the authors applied a convolutional long short-term memory RNN to extract 3D vascular centerlines of endothelial cells. Their approach was based on the U-net architecture [23], which is a well-known fully convolutional network [24] widely used for biomedical image segmentation. Bates and colleagues achieved state-of-the-art results in terms of centerline extraction; nevertheless, they reported that certain vessels in the images were combined in the automatic segmentation.

3. Data and Methods

The proposed vasculature segmentation method for 3D *in vivo* MPM images, *DeepVess*, consists of (i) pre-processing to remove *in vivo* physiological motion artifacts due to respiration and heartbeat, (ii) applying a 3D CNN for binary segmentation of the vessel tree, and (iii) post-processing to remove artifacts such as network discontinuities and holes.

3.1. Data

3.1.1. Animals

All animal procedures were approved by the Cornell University Institutional Animal Care and Use Committee and were performed under the guidance of the Cornell Center for Animal Resources and Education. We used double transgenic mice (B6.Cg-Tg (APP^{swe}, PSEN1^{dE9}) 85Dbo/J, referred to as APP/PS1 mice) that express two human proteins associated with early onset AD, a chimeric mouse/ human amyloid precursor protein (Mo/HuAPP695^{swe}) and a mutant human presenilin1 (PS1-dE9), which is a standard model of AD and typically develops amyloid-beta plaque deposition around 6 months of age [25]. Littermate wild type (WT) mice (C57BL/6) served as controls. Animals were of both

sexes and ranged in age from 18 to 31 weeks for young mice and from 50 to 64 weeks for the old mice (6 WT and 6 AD at each age, for a total of 24 mice).

3.1.2. *In vivo imaging of cortical vasculature*

We use a locally-designed multiphoton microscope [26] for *in vivo* imaging of the brain vasculature. Glass-covered craniotomies were prepared over parietal cortex, as described previously [27, 28]. We waited at least three weeks after the surgery before imaging to give time for the mild surgically-induced inflammation to subside. Windows typically remained clear for as long as 20 weeks. This technique allows us to map the architecture of the vasculature throughout the top 500 μm of the cortex. Briefly, the blood plasma of an anesthetized mouse was labeled with an intravenous injection of Texas Red labeled dextran (70 KDa, Life Technologies). The two-photon excited fluorescence intensity was recorded while the position of the focus of a femtosecond laser pulse train was scanned throughout the brain, providing a three-dimensional image of the vasculature [26]. Imaging was done using 800-nm or 830-nm, 75-fs pulses from a Ti:Sapphire laser oscillator (MIRA HP, pumped by a Verdi-V18, or Vision S, Coherent). Lasers were scanned by galvanometric scanners and focused into the sample using a 1.0 NA, 20X water-immersion objective lens (Carl Zeiss, Inc.). Image stacks were acquired with 645/45 nm (center wavelength/bandwidth) bandpass filters. The ScanImage software package [29] was used to control the whole system. Image stacks were taken with a range of magnifications resulting in lateral voxel sizes from 0.45 to 1.71 $\mu\text{m}/\text{pixel}$, but always 1 μm in the axial direction. Finally, the images were resampled to have voxel size of 1 μm cube.

3.1.3. *Expert annotation*

We implemented a protocol to facilitate the manual 3D segmentation task using ImageJ, an open-source image processing software package [30] (supplementary material). Two people, one expert and one less experienced, each manually segmented a motion artifact corrected (see below), $256 \times 256 \times 200$ voxel image, independently, which took about 20 and 30 hours, respectively. The sec-

ond annotator was trained by the expert and then had several months of practice prior to performing this task. These data were used to estimate inter-human segmentation variation. We treated the expert labels as the “gold standard” segmentation and used the second annotator’s labels to compare variability in manual segmentation. All other comparisons were made with respect to the gold standard segmentation as the ground truth. This dataset was divided into training, validation, and testing datasets (50%-25%-25%). The training and validation datasets were used in the optimization of CNN architectures, while the test dataset was kept unused until the end of architecture design process and used for the final unbiased evaluation.

3.2. Preprocessing

Motion artifacts caused by physiological movements are one of the major challenges for 3D segmentation of *in vivo* MPM images. Furthermore, global linear transformation models cannot compensate for the local nonuniform motion artifacts, for example, due to a breath occurring part way through the raster scanning for an MPM image. In this study, we adopted the non-rigid non-parametric diffeomorphic demons image registration tool implemented based on the work of Thirion [31] and Vercauteren et al. [32]. Our approach is to register each slice to the previous slice, starting from the first slice as the fixed reference. The diffeomorphic demons algorithm aims to match the intensity values between the reference image and deformed image, where cost is computed as the mean squared error. The smoothness prior on the deformation field is implemented via an efficient Gaussian smoothing of gradient fields, and invertability is ensured via concatenation of small deformations. A Gaussian kernel with the standard deviation of 1.3 was chosen based on our empirical tests with MPM images.

3.3. Convolutional Neural Network Architectures

Our aim in this work is to design a system that takes an input stack of images (in 3D) and produces a segmentation of vessels as a binary volume

of the same size. For this task, as we elaborate below, we explored different CNN architectures using validation performance as our guiding metric. Our baseline CNN architecture starts with a 3D input image patch (tile), which has $33 \times 33 \times 5$ voxels (in x, y, and z directions). The first convolution layer uses a $7 \times 7 \times 5$ voxel kernel with 32 features to capture 3D structural information within the neighborhood of the targeted voxel. The output of this layer, 32 nodes of $27 \times 27 \times 1$ voxel images, enter a max pooling layer with a 2×2 kernel and 2×2 strides. Another convolution layer with $5 \times 5 \times 1$ kernel and 64 features, followed by a similar max pooling layer are then applied before the application of the fully connected dense layer with 1024 hidden nodes and dropout [33] with a probability value of 50%. The output is a two-node layer, which represents the probability that the pixel at the center of the input patch belongs to tissue vs. vessel. The CNN takes an input 3D patch and produces a segmentation label for the central voxel. All the convolution layers have a bias term and rectified linear unit (ReLU) as the element-wise nonlinear activation function.

Different kernel sizes for the 3D convolution layers were explored in our experiments. Note that each choice in the architecture parameters (including the kernel size) corresponded to a different input patch size. As the validation results summarized in Table S2 indicate, the best performing baseline architecture had a 3D convolution layer with a $7 \times 7 \times 7$ voxel kernel and an input patch size of $33 \times 33 \times 7$. Based on this result we chose an input patch size of $33 \times 33 \times 7$ as the optimal field of view (FOV) for segmentation. We then explored the effect of the number of convolutional and max pooling layers. As summarized in Table S3, the best architecture had three 3D convolution layers with a $3 \times 3 \times 3$ voxel kernel, a max pooling layer, followed by two convolution layers with a 3×3 voxel kernel, a max pooling layer, and a fully connected neural network with a 1024-node hidden layer and FOV of $33 \times 33 \times 7$. The performance was improved further when the output is the segmentation of the central $5 \times 5 \times 1$ patch and not just a single voxel. A larger output area has the advantage of accounting for the structural relationship between adjacent voxels in their segmentation. The optimal CNN architecture scheme is shown in Figure 1.

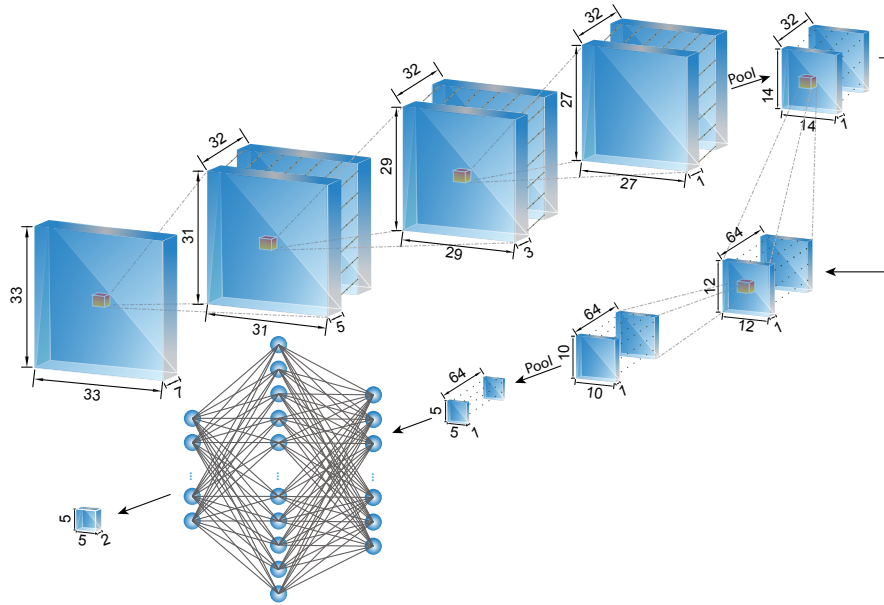


Figure 1: The optimal 3D CNN architecture. The field of view (FOV), i.e. the input patch size, is $33 \times 33 \times 7$ voxels and the output is the segmentation of the $5 \times 5 \times 1$ patch (region of interest, ROI) at the center of the patch. The convolution kernels are $3 \times 3 \times 3$ voxels for all the layers and ReLU is used as the element-wise nonlinear activation function. The first three convolution layers have 32 channels and are followed by pooling. The second three convolution layers have 64 channels. The output of convolution layers is $5 \times 5 \times 1$ voxels with 64 channels, which is fed to a fully connected neural network with a 1024-node hidden layer. The final result has $5 \times 5 \times 1$ voxels with two channels representing the probability of the foreground and background label associations.

3.4. Performance metrics

There are different performance metrics to compare agreement between an automated segmentation method and a “ground truth” (GT) human annotation. In the context of binary segmentation, the foreground (F) will be the positive class, and the negative class will correspond to the background (B). Therefore, true positive (TP) can be measured as the total number of voxels where both the automatic and human segmentation labels are foreground. True Negative (TN), False Positive (FP) and False Negative (FN) can be defined in a similar fashion.

Based on these, we can compute *sensitivity*, *specificity*, and *precision*. For example, sensitivity is the percentage of GT foreground voxels that are labeled by the automatic segmentation (ASeg) correctly. Mathematically, we have:

$$\text{sensitivity} = P(y = F | GT = F) = \frac{TP}{TP + FN} \quad (1)$$

$$\text{specificity} = P(y = B | GT = B) = \frac{TN}{TN + FP} \quad (2)$$

$$\text{precision} = P(GT = F | y = F) = \frac{TP}{TP + FP} \quad (3)$$

The *Dice coefficient* (DC), *Jaccard index* (JI), and *modified Hausdorff distance* (MHD) are another set of commonly used segmentation performance metrics. JI is defined as the ratio between the number of voxels labeled as foreground by both GT and ASeg, to the total number of voxels that are called foreground by either GT and ASeg. DC is very similar to JI, except it values TP twice as much as FP and FN. JI and DC are useful metrics when the number of the foreground voxels is much less than background and the detection accuracy of the foreground voxels is more important compared to background voxel detection, which is the case for 3D imaging of vasculature.

$$JI = P(y = F \cap GT = F | y = F \cup GT = F) = \frac{TP}{TP + FP + FN} \quad (4)$$

$$DC = \frac{2 \times JI}{1 + JI} = \frac{2 \times TP}{2 \times TP + FP + FN} \quad (5)$$

On the other hand, MHD [34] quantifies accuracy in terms of distances between boundaries, which might be appropriate when considering tubular structures.

For each boundary point in image \mathbf{A} ($a \in \mathcal{A}$), the closest Euclidean distance ($d(a, b) = \|a - b\|_2$) to any boundary point inside image \mathbf{B} ($b \in \mathcal{B}$) is first calculated, $d(a, \mathcal{B}) = \min_{b \in \mathcal{B}} \|a - b\|_2$. This is then averaged over all boundary points in \mathcal{A} : $\frac{1}{N_a} \sum_{a \in \mathcal{A}} d(a, \mathcal{B})$ [35]. MHD is then defined as:

$$MHD = \max \left[\frac{1}{N_a} \sum_{a \in \mathcal{A}} d(a, \mathcal{B}), \frac{1}{N_b} \sum_{b \in \mathcal{B}} d(b, \mathcal{A}) \right] \quad (6)$$

$$d(a, \mathcal{B}) = \min_{b \in \mathcal{B}} \|a - b\|_2 \quad (7)$$

Note that in the segmentation setting, \mathbf{A} and \mathbf{B} can represent the foreground boundaries in the automatic and GT segmentations, respectively. Finally, we can compute the MHD on centerlines instead of boundaries, a metric we call MHD-CL.

3.5. Training and implementation details

In training our segmentation algorithms, we used the cross-entropy loss function, defined as:

$$Loss = \sum_{i \in \{TP, FP, FN\}} - [y_i \log(p_i) + (1 - y_i) \log(1 - p_i)] \quad (8)$$

y_i is the GT label and p_i is the model’s output as the probability of the target voxel i belonging to the foreground. We trained our model using *Adam* stochastic optimization [36] with a learning rate of 10^{-4} for 100 epochs during architecture exploration and a learning rate of 10^{-6} for 30,000 epochs during the fine tuning of model parameters for the proposed architecture with mini-batch size of 1000 samples. The fine tuning took one month on one NVIDIA TITAN X GPU. We implemented our models in Python using TensorflowTM [37].

3.6. Post-processing

CNN segmentation results contain some segmentation artifact such as holes inside the vessels, rough boundaries, or isolated small objects. In order to remove these artifacts, the holes within the vessels were filled. This was followed by application of a 3D mean filter with a $3 \times 3 \times 3$ voxel kernel and the removal

of small foreground objects, e.g. smaller than 100 voxels. This result was used to compare to the gold standard.

3.7. Analysis of experimental data sets

To characterize the cortical vasculature of the experimental animals, we identified capillary segments by calculating centerlines from the segmented image data. Our centerline extraction method includes dilation and thinning operations, in addition to some centerline artifact removal steps. The binary segmentation image was first thinned using the algorithm developed by Lee et al. [38]. The result was then dilated using a spherical kernel with a radius of 5-voxels to improve the vessel connectivity, which was followed by mean filtering with a $3 \times 3 \times 3$ voxel kernel and removing holes from each cross section. Next, a thinning step was applied again to obtain the new centerline result. The original segmented image was dilated using a spherical kernel with a radius of 1-voxel to act as the mask for the centerlines with the goal of improving the centerline connectivity. The following rules were applied to the resulting centerlines repeatedly until no further changes could be done. A vessel is a segment between two bifurcations.

1. Remove any vessels with one dead-end, which are not connected to the network, and with length smaller than 11 voxels.
2. Remove single voxels connected to a junction.
3. Remove single voxels with no connections.
4. Remove vessel loops with length of one or two voxels.

Finally, the centerline network representation (i.e. nodes, edges, and their properties) was extracted.

4. Results

We conducted a systematic evaluation of several network architecture parameters in order to optimize segmentation accuracy of images of mouse cortex vasculature from MPM. We emphasize that this exploration was all based on

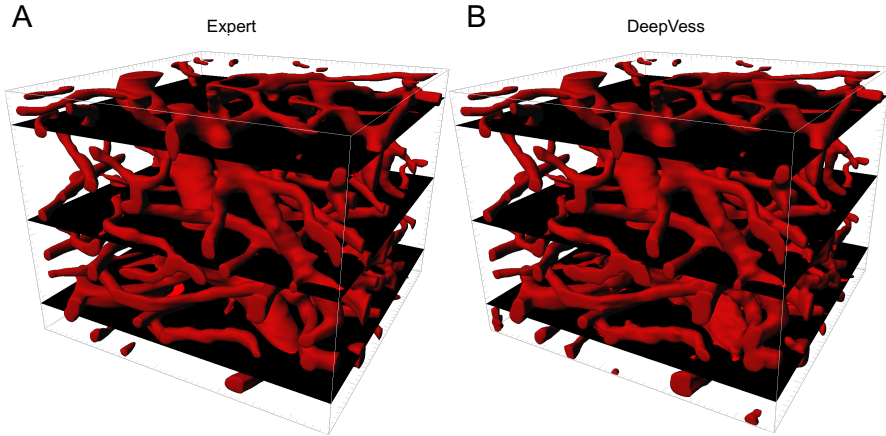


Figure 2: 3D rendering of (A) the expert’s manual and (B) *DeepVess* segmentation results. The top, middle, and bottom black plains correspond to the high, medium, and low quality examples, respectively, which are analyzed further in the Discussion (Figure 5). Each volume is $292 \times 292 \times 200 \mu m^3$

performance on the validation dataset and the final results presented reflect the model accuracy on an independent test dataset. The detailed performance results for some of the tested architectures are reported in Tables S2 and S3. The optimal architecture, *DeepVess*, was trained on the training data until the model accuracy stopped improving and no overfitting was observed (30,000 epochs). Figure S1 shows the JI learning curve over 30,000 epochs, for training, validation, and test datasets. The constant gap between JI of the training and validation datasets, which represent generalization error, confirms that we are not overfitting.

Furthermore, we implemented the-state-of-the-art method of Teikari et al. [21], and improved it by changing the 2D convolutional kernels into 3D kernels, based on the suggestion in the Discussion of their paper. Table 1 summarizes the comparison between the performance of our optimal architecture on the test dataset and the improved state-of-the-art as well as the inter-human variability. These results, as well as Figure S1 demonstrate that *DeepVess* outperforms both the state-of-the-art method [21] and the trained human annotator on the

Table 1: The results of our proposed CNN architecture vs. manual annotation by a trained person and the state-of-the-art (Teikari et al. [21]) compared to the gold standard of the expert human annotation. CNN surpass both of them in terms of sensitivity, Dice index, Jaccard index, and boundary modified Hausdorff distance (MHD).

	<i>Sensitivity</i>	<i>Specificity</i>	<i>Precision</i>	<i>Dice</i>	<i>Jaccard</i>	<i>MHD</i>
Human annotator	85.59%	98.59%	84.05%	84.82%	73.64%	1.19
Teikari et al. [21]	86.89%	98.94%	88.06%	87.48%	77.74%	1.49
<i>DeepVess</i>	95.09%	98.47%	84.80%	89.65%	81.24%	1.04

test dataset.

We next examined the quality of the vessel centerlines derived from the different segmentations. Using the centerline modified Hausdorff distance (CL MHD) as a centerline extraction accuracy metric, *DeepVess* (CL MHD [*DeepVess*] = 3.03) is substantially better than the state-of-the-art Teikari et al. method (CL MHD [Teikari et al.] = 3.72). But there is still room for improvement in terms of automatic centerline extraction as neither automatic methods yielded scores as good as the trained human annotator (CL MHD [human annotator] = 2.73).

In MPM, the variation in the signal to noise as a function of imaging depth leads to changes in image quality between image slices. The performance of a segmentation method should therefore be assessed by analyzing slices separately. Figure 3 illustrates the boxplot of slice-wise DI values from the x-y planes within the 3D MPM image dataset. *DeepVess* had a higher DI in comparison to the Teikari et al. and the trained annotator’s results. However, there was more variation compared to the other two results, which implies the possibility and need for further improvements.

4.1. Capillary alteration caused by aging and Alzheimer’s disease

Strong correlations between vascular health, brain blood flow and AD suggest that mapping the microvascular network is critical to the understanding of cognitive health in aging [39]. To explore this question, we imaged the cortical vascular networks in young and old mouse models of AD (young AD and old AD) and their young and old wild type littermates (young WT and old WT).

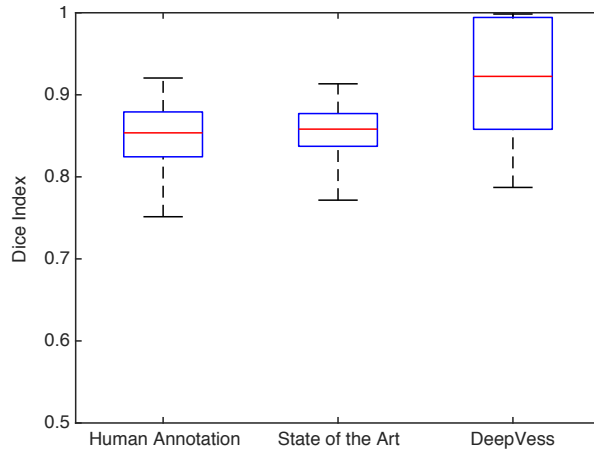


Figure 3: Slice-wise Dice Index of *DeepVess* vs. manual annotation by a trained person and the state-of-the-art (Teikari et al. [21]) compared to the gold standard of the expert human annotation. The central red mark is the median, and the top and bottom of the box is the third and first quartiles, respectively. The whiskers indicates the range of data. *DeepVess* has higher median value in comparison to the Teikari et al. and the human annotator (Wilcoxon signed-rank test, $p = 2.98e - 23$ and $p = 2.8e - 28$, respectively).

Imaged volumes ranged from 230×230 to $600 \times 600 \mu m^2$ in x-y and 130 to $459 \mu m$ in the z direction. We imaged 6 animals per group, with at least 3000 capillary segments analyzed for each group.

The resulting 3D stacks of images were preprocessed, segmented with *DeepVess*, and post-processed as discussed in the previous sections. Centerlines were extracted and individual vessel segments were identified. To analyze capillaries while excluding arterioles and venules, only vessel segments less than $10 \mu m$ in diameter were included. Three metrics were selected to characterize the vascular network. For each capillary segment, we calculated the diameter averaged along the length (Figure 4.A), the length (Figure 4.B), and the tortuosity, defined as the length divided by the Euclidean distance between the two ends (Figure 4.C). The distributions of capillary diameter, length, and tortuosity varied little between young and old mice or between WT and AD genotype (Table S1). There were subtle shifts ($\sim 0.25 \mu m$) in the diameter distribution between groups, but no clear trend across old/young or WT/AD. However, we observed a systematic

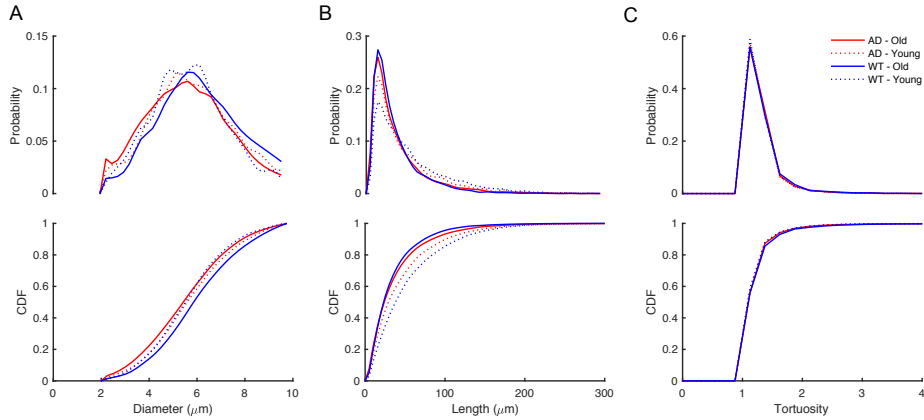


Figure 4: Comparison of capillaries between young and old mice with WT and AD genotype. The relative probability and Cumulative distribution function (CDF) of the (A) diameters, (B) length, and (C) tortuosity based on all capillaries aggregated within each of the four groups. We compared these metrics between the groups using Kruskal-Wallis test followed by Bonferroni multiple comparison correction [40] (Table S1).

decrease in the number of longer length ($> 75\mu m$) capillaries in older animals as compared to young in both WT and AD mice.

5. Discussion

The segmentation of 3D vasculature images is a laborious task that slows down the progress of biomedical research and constrains the use of imaging in clinical practice. There has been significant research into tackling this problem via image analysis methods that reduce or eliminate human involvement. In this work, we presented a CNN approach, which surpasses the state-of-the-art vessel segmentation method [21] as well as a trained human annotator. The proposed algorithm, *DeepVess*, segments 3D *in vivo* vascular MPM image with ten million voxel in ten minutes using one NVIDIA TITAN X GPU, a task that takes 30 hours for a trained human annotator to complete manually. *DeepVess* implements pre- and post-processing tools to deal with *in vivo* MPM images that suffer from different motion artifacts. *DeepVess* is freely available at <https://github.com/mh973/DeepVess> and can be used immediately by

researchers who use MPM for vasculature imaging. Also, our model can be fine-tuned further with training samples for other 3D vasiform structures or other imaging modalities.

In order to characterize the performance of *DeepVess*, we compared the automated segmentation to the expert manual segmentation (Figure 2). We selected three slices with different qualities of segmentation results. The 3D rendering of the mouse brain vasculature shown in Figure 2 indicates the location of these top, middle, and bottom slices representing typical high, medium, and low segmentation quality, respectively. To quantify the uncertainty in the automated segmentation, we used 50% dropout during test-time [41] and computed Shannon’s entropy at each voxel. Higher entropy represents higher segmentation uncertainty at a particular voxel. The entropy results together with the comparison between *DeepVess* and the expert segmentations for those three planes are illustrated in Figure 5. The left column contains the intensity gray-scale images of these examples. The segmentation results of the *DeepVess* and the expert are overlapped on the original gray-scale image with red (*DeepVess*) and green (the expert), as shown in the middle column. Yellow represents agreement between *DeepVess* and the expert. The right column shows the entropy of each example estimated via test time dropout. We observe that, in general, *DeepVess* has higher uncertainty at the boundaries of vessels. The disagreement with ground truth is also mostly concentrated at the boundaries. Images from deeper slides within the brain tissue that often have lower image quality and higher noise levels due to the nature of MPM, suffer from more segmentation errors. These images can often be challenging even for expert humans. Arrows in Figure 5.C highlight examples of these difficulties. The error example 1 illustrates the case where the expert ignored bright pixels around the vessel lumen based on their knowledge of the underlying physiology and experience with MPM images of brain that postulate a rounded lumen instead of a jittery and rough lumen, despite a very strong signal. The error example 2 illustrates a low intensity vessel junction that was judged to be artifact by humans based on experience or information from other image planes. The error example 3

illustrates the case where a small vessel does not exhibit a strong signal and it is not connected to another major vessel.

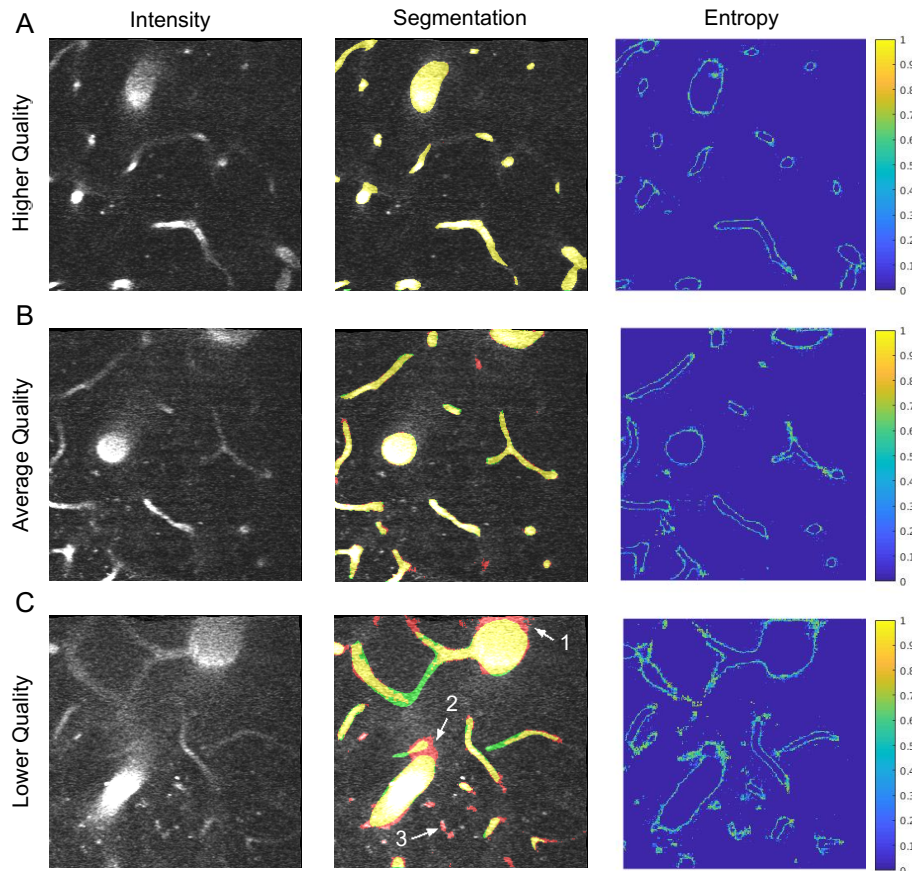


Figure 5: Comparison of *DeepVess* and the gold standard human expert segmentation results in image planes as shown in Figure 2. Imaging is generally higher quality at planes closer to the sample surface. (Left column) Image intensity shown with gray scale after motion artifact removal. The dark spots within the vessels are red blood cells that do not take up the injected dye. (Middle column) Comparison between CNN (red) and the expert (green) segmentation results overlaid on images. Yellow shows agreement between the two segmentations. (Right column) Shannon entropy, which is a metric of CNN segmentation uncertainty using 50% dropout at the test-time [41]. The boundaries of vessels with high entropy values, shown in warmer colors, demonstrate the uncertainty of CNN results at those locations.

5.1. Aging and Alzheimer’s disease have little effect on capillary characteristics

In vivo imaging with multiphoton microscopy of capillary beds is free of distortions in vessel structure caused by postmortem tissue processing that can result in artifacts such as altered diameters[5]. However, the images often suffer from poor signal to noise and motion artifacts. An additional challenge is that unlabeled, moving red blood cells in the vessel lumen cause dark spots and streaks that move over time. Disease models are often especially challenging because inflammation and tissue damage can further degrade imaging conditions. The segmentation method developed in this work provides robust and efficient analysis which enabled us to quantify and compare capillary diameters and other vascular parameters from *in vivo* cortex images across multiple animals, with varying age as well as across WT mice and AD models. Many studies have shown anatomical and physiological differences in microvasculature associated both with age and AD, such as changes in composition of large vessel walls’ smooth muscles [42], increased collagen VI in microvascular basement membranes and their thickening in AD [43], and age-associated reduction of microvascular plasticity and the ability of the vessels to respond appropriately to changes in metabolic demand [44]. For the vascular parameters of segment length, diameter, and tortuosity considered here, previous work has shown that AD mouse models have increased tortuosity in cortical penetrating arterioles as compared to WT mice [45, 46]. Our analysis of capillaries excluded these vessels.

Using a very large database of vessel segments measured in three dimensions, we surprisingly found very little difference in capillary diameter or tortuosity between young and old animals or between wild type and AD mouse models. There was a decrease in the number of long capillary segments in the aged animals compared to young in both the wild type and AD groups. These finding may not generalize across all ages and mouse models of AD. Sonntag et al. [1] argue that changes in vasculature due to aging might be non-linear and multiphasic. For instance, two studies showed that the capillary density increases during adulthood and then declines in more advanced age [47, 48]. Several pre-

vious studies have characterized the average diameters of cortical capillaries in mice, as summarized in Table 2. There are a wide range of imaging approaches used in these various studies and data from both live animal and postmortem analysis is included. It is possible that some of these differences emerge when tissues are processed rather than measured *in vivo* as was done here. Studies based on sectioned tissue sample the 3D vascular architecture differently so it is difficult to make direct comparisons between datasets. Measures of capillaries depend on the definition of capillaries, here was based on a threshold diameter of $10\mu m$, which could explain some of the variability in the literature. Not surprisingly given the differences in approach and sample preparation, there is significant disagreement between reported average diameters. Some differences may, however, reflect differences in vasculature across strains and ages of animals. Therefore, the proposed fully automated objective segmentation of 3D *in vivo* images of the vasculature can be used to reduce the variability due to sample preparation and imaging/analysis approach, allowing such strain and age differences to be elucidated clearly.

While *DeepVess* offers very high accuracy in the problem we consider, there is room for further improvement and validation, in particular in the application to other vasiform structures and modalities. For example, other types of (e.g., non-convolutional) architectures such as long short-term memory (LSTM) can be examined for this problem. Likewise, a combined approach that treats segmentation and centerline extraction methods together, such as the method proposed by Bates et al. [22] in a single complete end-to-end learning framework might achieve higher centerline accuracy levels.

6. Conclusions

Here, we presented *DeepVess*, a 3D CNN segmentation method with essential pre- and post-processing steps, to fully automate the vascular segmentation of 3D *in vivo* MPM images of murine brain vasculature. *DeepVess* promises to expedite biomedical research findings about the differences in angioarchitecture

Table 2: Comparison of measured mouse capillary diameters from different studies.

Study	Year	Background	Trans-gene	Phenotype	Age (week)	Imaging Modality	Vessel Diameter
This Study	2018	C57/BL6	APP/PS1	WT	18-31	<i>in vivo</i> 2PEF	$5.81 \pm 1.62 \mu\text{m}$
This Study	2018	C57/BL6	APP/PS1	WT	50-64	<i>in vivo</i> 2PEF	$6.19 \pm 1.76 \mu\text{m}$
This Study	2018	C57/BL6	APP/PS1	AD	18-31	<i>in vivo</i> 2PEF	$5.92 \pm 1.76 \mu\text{m}$
This Study	2018	C57/BL6	APP/PS1	AD	50-64	<i>in vivo</i> 2PEF	$5.71 \pm 1.77 \mu\text{m}$
Boero et al.[49]	1999	BALB/C	-	WT	11	<i>in vitro</i> optical imaging	$2.48 - 2.70 \mu\text{m}$
Drew et al. [50]	2011	C57/BL6	-	WT	-	<i>in vivo</i> 2PEF	$2.9 \pm 0.5 \mu\text{m}$
Blinder et al.[5]	2013	C57/BL6	-	WT	-	<i>in vivo</i> optical img., <i>in vitro</i> 2PEF	$2 - 5.3 \mu\text{m}$
Hall et al. [51]	2014	C57/BL6J	NG2-DsRed	WT	-	<i>in vivo</i> 2PEF	$4.4 \pm 0.1 \mu\text{m}$
Gutierrez-Jimenez[52]	2016	C57/BL6	NTac	WT	13-15	<i>in vivo</i> 2PEF	$4.1 - 4.5 \mu\text{m}$
Cudmore et al.[53]	2016	C57/BL6	Tie2-Cre :mTmG	WT	13-21, 64, 97	<i>in vivo</i> 2PEF	$5.03 \pm 1.18 \mu\text{m}$
Meyer et al.[54]	2008	C57/BL6	APP23	WT / AD	12-108	<i>in vitro</i> histology	$4 - 6 \mu\text{m}$
Tsai et al.[11]	2009	Swiss	-	WT	-	<i>in vivo</i> 2PEF	$3.97 - 4.11 \mu\text{m}$
Tsai et al.[11]	2009	C57/BL6	-	WT	-	<i>in vivo</i> 2PEF	$3.97 - 4.11 \mu\text{m}$
Heinzer et al.[55]	2004	C57/BL6	APP23	WT	52	MRA	$14 \pm 5 \mu\text{m}$
Heinzer et al.[55]	2004	C57/BL6	APP23	AD	52	MRA	$14 \pm 5 \mu\text{m}$
Heinzer et al.[56]	2006	C57/BL6	APP23	AD	44	<i>SRμCT</i>	$8.9 \mu\text{m}$
Heinzer et al.[57]	2007	C57/BL6	C3H/He:NSE- VEGF ₁₆₅₁	WT	16	<i>SRμCT</i>	$5.6 \pm 27.9 \mu\text{m}$
Heinzer et al.[57]	2007	C57/BL6	C3H/He:NSE- VEGF ₁₆₅₁	VEGF ₁₆₅	16	<i>SRμCT</i>	$5.5 \pm 29.3 \mu\text{m}$
Serduc et al. [58]	2006	Swiss nude	-	WT	5	<i>in vivo</i> 2PEF	$4 - 6 \mu\text{m}$
Verant et al. [59]	2007	Swiss nude	-	WT	5	<i>in vivo</i> 2PEF	$8.2 \pm 1.4 \mu\text{m}$

and the impact of such differences by removing the laborious and time consuming manual segmentation task from those process and analysis pipelines in addition to elimination of subjective image analysis results. We hope the availability of our open source code and reported results will facilitate and motivate the adoption of this method by researchers and practitioners.

References

References

- [1] W. E. Sonntag, D. M. Eckman, J. Ingraham, D. R. Riddle, Regulation of cerebrovascular aging, in: D. R. Riddle (Ed.), *Brain aging: models, methods, and mechanisms*, CRC Press/Taylor & Francis, Boca Raton, FL, 2007, Ch. 12, pp. 279–304.
- [2] K. Hossmann, Viability thresholds and the penumbra of focal ischemia, *Annals of neurology* 36 (4) (1994) 557–565.
- [3] L. Lin, J. Yao, R. Zhang, C.-C. Chen, C.-H. Huang, Y. Li, L. Wang, W. Chapman, J. Zou, L. V. Wang, High-speed photoacoustic microscopy of mouse cortical microhemodynamics, *Journal of biophotonics* 10 (6-7) (2017) 792–798.
- [4] Ş. E. Erdener, J. Tang, A. Sajjadi, K. Kılıç, S. Kura, C. B. Schaffer, D. A. Boas, Spatio-temporal dynamics of cerebral capillary segments with stalling red blood cells, *Journal of Cerebral Blood Flow & Metabolism* (2017) 0271678X17743877.
- [5] P. Blinder, P. S. Tsai, J. P. Kaufhold, P. M. Knutsen, H. Suhl, D. Kleinfeld, The cortical angiome: an interconnected vascular network with noncolumnar patterns of blood flow, *Nature neuroscience* 16 (7) (2013) 889–897.
- [6] J. C. Cruz Hernandez, O. Bracko, C. J. Kersbergen, V. Muse, M. Haft-Javaherian, M. Berg, L. Park, L. K. Vinarcsik, I. Ivasyk, Y. Kang, M. Cortes-Canteli, M. Peyrounette, V. Doyeux, A. Smith, J. Zhou,

- G. Otte, J. D. Beverly, E. Davenport, Y. Davit, S. Strickland, C. Iadecola, S. Lorthois, N. Nishimura, C. B. Schaffer, Neutrophil adhesion in brain capillaries contributes to cortical blood flow decreases and impaired memory function in a mouse model of alzheimer's disease, *bioRxiv* <https://www.biorxiv.org/content/early/2017/11/29/226886.full.pdf>, doi: 10.1101/226886.
- [7] C. Kirbas, F. Quek, A review of vessel extraction techniques and algorithms, *ACM Computing Surveys (CSUR)* 36 (2) (2004) 81–121.
- [8] D. Lesage, E. D. Angelini, I. Bloch, G. Funka-Lea, A review of 3d vessel lumen segmentation techniques: Models, features and extraction schemes, *Medical image analysis* 13 (6) (2009) 819–845.
- [9] G. Litjens, T. Kooi, B. E. Bejnordi, A. A. A. Setio, F. Ciompi, M. Ghafoorian, J. A. van der Laak, B. van Ginneken, C. I. Snchez, A survey on deep learning in medical image analysis, *Medical Image Analysis* 42 (Supplement C) (2017) 60 – 88.
- [10] M. M. Fraz, P. Remagnino, A. Hoppe, B. Uyyanonvara, A. R. Rudnicka, C. G. Owen, S. A. Barman, Blood vessel segmentation methodologies in retinal images—a survey, *Computer methods and programs in biomedicine* 108 (1) (2012) 407–433.
- [11] P. S. Tsai, J. P. Kaufhold, P. Blinder, B. Friedman, P. J. Drew, H. J. Karten, P. D. Lyden, D. Kleinfeld, Correlations of neuronal and microvascular densities in murine cortex revealed by direct counting and colocalization of nuclei and vessels, *Journal of Neuroscience* 29 (46) (2009) 14553–14570.
- [12] J. Yi, J. B. Ra, A locally adaptive region growing algorithm for vascular segmentation, *International Journal of Imaging Systems and Technology* 13 (4) (2003) 208–214.
- [13] J. Mille, L. D. Cohen, Deformable tree models for 2d and 3d branching structures extraction, in: *Computer Vision and Pattern Recognition Work-*

- shops, 2009. CVPR Workshops 2009. IEEE Computer Society Conference on, IEEE, 2009, pp. 149–156.
- [14] V. Gulshan, L. Peng, M. Coram, M. C. Stumpe, D. Wu, A. Narayanaswamy, S. Venugopalan, K. Widner, T. Madams, J. Cuadros, et al., Development and validation of a deep learning algorithm for detection of diabetic retinopathy in retinal fundus photographs, *Jama* 316 (22) (2016) 2402–2410.
- [15] C. Szegedy, V. Vanhoucke, S. Ioffe, J. Shlens, Z. Wojna, Rethinking the inception architecture for computer vision, in: *Proceedings of the IEEE Conference on Computer Vision and Pattern Recognition*, 2016, pp. 2818–2826.
- [16] A. Wu, Z. Xu, M. Gao, M. Buty, D. J. Mollura, Deep vessel tracking: A generalized probabilistic approach via deep learning, in: *Biomedical Imaging (ISBI), 2016 IEEE 13th International Symposium on*, IEEE, 2016, pp. 1363–1367.
- [17] H. Fu, Y. Xu, D. W. K. Wong, J. Liu, Retinal vessel segmentation via deep learning network and fully-connected conditional random fields, in: *Biomedical Imaging (ISBI), 2016 IEEE 13th International Symposium on*, IEEE, 2016, pp. 698–701.
- [18] H. Fu, Y. Xu, S. Lin, D. W. K. Wong, J. Liu, Deepvessel: Retinal vessel segmentation via deep learning and conditional random field, in: *International Conference on Medical Image Computing and Computer-Assisted Intervention*, Springer, 2016, pp. 132–139.
- [19] K.-K. Maninis, J. Pont-Tuset, P. Arbeláez, L. Van Gool, Deep retinal image understanding, in: *International Conference on Medical Image Computing and Computer-Assisted Intervention*, Springer, 2016, pp. 140–148.
- [20] S. Lorthois, F. Lauwers, F. Cassot, Tortuosity and other vessel attributes

- for arterioles and venules of the human cerebral cortex, *Microvascular research* 91 (2014) 99–109.
- [21] P. Teikari, M. Santos, C. Poon, K. Hynynen, Deep learning convolutional networks for multiphoton microscopy vasculature segmentation, arXiv preprint arXiv:1606.02382.
- [22] R. Bates, B. Irving, B. Markelc, J. Kaeppler, G. Brown, R. J. Muschel, M. Brady, V. Grau, J. A. Schnabel, Segmentation of vasculature from fluorescently labeled endothelial cells in multi-photon microscopy images, *IEEE Transactions on Medical Imaging*.
- [23] O. Ronneberger, P. Fischer, T. Brox, U-net: Convolutional networks for biomedical image segmentation, in: *International Conference on Medical Image Computing and Computer-Assisted Intervention*, Springer, 2015, pp. 234–241.
- [24] J. Long, E. Shelhamer, T. Darrell, Fully convolutional networks for semantic segmentation, in: *Proceedings of the IEEE Conference on Computer Vision and Pattern Recognition*, 2015, pp. 3431–3440.
- [25] J. L. Jankowsky, D. J. Fadale, J. Anderson, G. M. Xu, V. Gonzales, N. A. Jenkins, N. G. Copeland, M. K. Lee, L. H. Younkin, S. L. Wagner, et al., Mutant presenilins specifically elevate the levels of the 42 residue β -amyloid peptide in vivo: evidence for augmentation of a 42-specific γ secretase, *Human molecular genetics* 13 (2) (2003) 159–170.
- [26] W. Denk, J. H. Strickler, W. W. Webb, et al., Two-photon laser scanning fluorescence microscopy, *Science* 248 (4951) (1990) 73–76.
- [27] A. Holtmaat, T. Bonhoeffer, D. K. Chow, J. Chuckowree, V. De Paola, S. B. Hofer, M. Hübener, T. Keck, G. Knott, W. C. A. Lee, et al., Long-term, high-resolution imaging in the mouse neocortex through a chronic cranial window, *Nature protocols* 4 (8) (2009) 1128–1144.

- [28] A. Y. Shih, J. D. Driscoll, P. J. Drew, N. Nishimura, C. B. Schaffer, D. Kleinfeld, Two-photon microscopy as a tool to study blood flow and neurovascular coupling in the rodent brain, *Journal of Cerebral Blood Flow & Metabolism* 32 (7) (2012) 1277–1309.
- [29] T. A. Pologruto, B. L. Sabatini, K. Svoboda, Scanimage: flexible software for operating laser scanning microscopes, *Biomedical engineering online* 2 (1) (2003) 13.
- [30] M. D. Abràmoff, P. J. Magalhães, S. J. Ram, Image processing with imagej, *Biophotonics international* 11 (7) (2004) 36–42.
- [31] J.-P. Thirion, Image matching as a diffusion process: an analogy with maxwell’s demons, *Medical image analysis* 2 (3) (1998) 243–260.
- [32] T. Vercauteren, X. Pennec, A. Perchant, N. Ayache, Diffeomorphic demons: Efficient non-parametric image registration, *NeuroImage* 45 (1) (2009) S61–S72.
- [33] N. Srivastava, G. E. Hinton, A. Krizhevsky, I. Sutskever, R. Salakhutdinov, Dropout: a simple way to prevent neural networks from overfitting., *Journal of machine learning research* 15 (1) (2014) 1929–1958.
- [34] M.-P. Dubuisson, A. K. Jain, A modified hausdorff distance for object matching, in: *Pattern Recognition, 1994. Vol. 1-Conference A: Computer Vision & Image Processing., Proceedings of the 12th IAPR International Conference on, Vol. 1, IEEE, 1994*, pp. 566–568.
- [35] D. P. Huttenlocher, G. A. Klanderman, W. J. Rucklidge, Comparing images using the hausdorff distance, *IEEE Transactions on pattern analysis and machine intelligence* 15 (9) (1993) 850–863.
- [36] D. Kingma, J. Ba, Adam: A method for stochastic optimization, *arXiv preprint arXiv:1412.6980*.

- [37] M. Abadi, A. Agarwal, P. Barham, E. Brevdo, Z. Chen, C. Citro, G. S. Corrado, A. Davis, J. Dean, M. Devin, et al., Tensorflow: Large-scale machine learning on heterogeneous distributed systems, arXiv preprint arXiv:1603.04467.
- [38] T.-C. Lee, R. L. Kashyap, C.-N. Chu, Building skeleton models via 3-d medial surface axis thinning algorithms, *CVGIP: Graphical Models and Image Processing* 56 (6) (1994) 462–478.
- [39] C. Iadecola, Neurovascular regulation in the normal brain and in alzheimer’s disease, *Nature reviews Neuroscience* 5 (5) (2004) 347.
- [40] G. A. Milliken, D. E. Johnson, *Analysis of messy data volume 1: designed experiments*, Vol. 1, CRC Press, 2009.
- [41] Y. Gal, Z. Ghahramani, Dropout as a bayesian approximation: Representing model uncertainty in deep learning, in: *international conference on machine learning*, 2016, pp. 1050–1059.
- [42] R. N. Kalaria, Cerebral vessels in ageing and alzheimer’s disease, *Pharmacology & therapeutics* 72 (3) (1996) 193–214.
- [43] E. Farkas, P. G. Luiten, Cerebral microvascular pathology in aging and alzheimer’s disease, *Progress in neurobiology* 64 (6) (2001) 575–611.
- [44] D. R. Riddle, W. E. Sonntag, R. J. Lichtenwalner, Microvascular plasticity in aging, *Ageing research reviews* 2 (2) (2003) 149–168.
- [45] A. Dorr, B. Sahota, L. V. Chinta, M. E. Brown, A. Y. Lai, K. Ma, C. A. Hawkes, J. McLaurin, B. Stefanovic, Amyloid- β -dependent compromise of microvascular structure and function in a model of alzheimers disease, *Brain* 135 (10) (2012) 3039–3050.
- [46] A. Y. Lai, A. Dorr, L. A. Thomason, M. M. Koletar, J. G. Sled, B. Stefanovic, J. McLaurin, Venular degeneration leads to vascular dysfunction in a transgenic model of alzheimers disease, *Brain* 138 (4) (2015) 1046–1058.

- [47] J. Wilkinson, J. Hopewell, H. Reinhold, A quantitative study of age-related changes in the vascular architecture of the rat cerebral cortex, *Neuropathology and applied neurobiology* 7 (6) (1981) 451–462.
- [48] O. Hunziker, S. Abdel'al, U. Schulz, The aging human cerebral cortex: a stereological characterization of changes in the capillary net, *Journal of gerontology* 34 (3) (1979) 345–350.
- [49] J. A. Boero, J. Ascher, A. Arregui, C. Rovainen, T. A. Woolsey, Increased brain capillaries in chronic hypoxia, *Journal of applied physiology* 86 (4) (1999) 1211–1219.
- [50] P. J. Drew, A. Y. Shih, D. Kleinfeld, Fluctuating and sensory-induced vasodynamics in rodent cortex extend arteriole capacity, *Proceedings of the National Academy of Sciences* 108 (20) (2011) 8473–8478.
- [51] C. N. Hall, C. Reynell, B. Gesslein, N. B. Hamilton, A. Mishra, B. A. Sutherland, F. M. O'Farrell, A. M. Buchan, M. Lauritzen, D. Attwell, Capillary pericytes regulate cerebral blood flow in health and disease, *Nature* 508 (7494) (2014) 55–60.
- [52] E. Gutiérrez-Jiménez, C. Cai, I. K. Mikkelsen, P. M. Rasmussen, H. Angleys, M. Merrild, K. Mouridsen, S. N. Jespersen, J. Lee, N. K. Iversen, et al., Effect of electrical forepaw stimulation on capillary transit-time heterogeneity (cth), *Journal of Cerebral Blood Flow & Metabolism* 36 (12) (2016) 2072–2086.
- [53] R. H. Cudmore, S. E. Dougherty, D. J. Linden, Cerebral vascular structure in the motor cortex of adult mice is stable and is not altered by voluntary exercise, *Journal of Cerebral Blood Flow & Metabolism* (2016) 0271678X16682508.
- [54] E. P. Meyer, A. Ulmann-Schuler, M. Staufenbiel, T. Krucker, Altered morphology and 3d architecture of brain vasculature in a mouse model

for alzheimer's disease, *Proceedings of the National Academy of Sciences* 105 (9) (2008) 3587–3592.

- [55] S. Heinzer, T. Krucker, M. Stampanoni, R. Abela, E. P. Meyer, A. Schuler, P. Schneider, R. Müller, U. Bonse, Hierarchical bioimaging and quantification of vasculature in disease models using corrosion casts and micro-computed tomography, in: *Proc. SPIE*, Vol. 5535, SPIE Bellingham, WA, USA, 2004, pp. 65–76.
- [56] S. Heinzer, T. Krucker, M. Stampanoni, R. Abela, E. P. Meyer, A. Schuler, P. Schneider, R. Müller, Hierarchical microimaging for multiscale analysis of large vascular networks, *Neuroimage* 32 (2) (2006) 626–636.
- [57] S. Heinzer, R. Müller, M. Stampanoni, R. Abela, E. P. Meyer, A. Ulmann-Schuler, T. Krucker, Computer-based analysis of microvascular alterations in a mouse model for alzheimer's disease, in: *Medical Imaging 2007: Physiology, Function, and Structure from Medical Images*, Vol. 6511, International Society for Optics and Photonics, 2007, p. 651104.
- [58] R. Serduc, P. Vérant, J.-C. Vial, R. Farion, L. Rocas, C. Rémy, T. Fadlallah, E. Brauer, A. Bravin, J. Laissue, et al., In vivo two-photon microscopy study of short-term effects of microbeam irradiation on normal mouse brain microvasculature, *International Journal of Radiation Oncology* Biology* Physics* 64 (5) (2006) 1519–1527.
- [59] P. Vérant, R. Serduc, B. Van Der Sanden, C. Rémy, J.-C. Vial, A direct method for measuring mouse capillary cortical blood volume using multiphoton laser scanning microscopy, *Journal of Cerebral Blood Flow & Metabolism* 27 (5) (2007) 1072–1081.

Supplementary materials

S1. Manual 3D segmentation protocol using ImageJ

First, we created a new *hyper-stack* (File menu→New) with 3D voxel size and bit depth similar to the original image (e.g. a 16-bit $1024 \times 1024 \times 500$ voxel hyper-stack). The original image and the new hyper-stack were then merged (Image menu → Color) into a multi-channel hyper-stack, which contained both the raw data and the segmentation results. On each image (in the x-y plane) the expert drew segmentation boundaries using the *free hand* tool and fill function (*F key*) while the second channel is selected using scrollbar. The *Color Picker* and *Channels Tool* (Image menu → Color) in addition to the Reverse CZT option (Edit menu → Options → Miscellaneous) was used to expedite the segmentation process.

Table S1: Comparison between metrics distributions between different groups using Kruskal-Wallis test followed by Bonferroni multiple comparison correction. $\Delta\mu$ is the difference between the mean values of the two tested groups.

	Diameter		Length		Tortuosity	
	$\Delta\mu$	P-value	$\Delta\mu$	P-value	$\Delta\mu$	P-value
AD-Old vs. AD-Young	0.206	2.61E-7	7.955	8.4E-22	0.016	0.798
AD-Old vs. WT-Old	0.475	2.93E-27	2.803	0.049	0.019	0.645
AD-Old vs. WT-Young	0.095	1.20E-5	16.14	4.6E-67	0.018	0.321
AD-Young vs. WT-Old	0.269	6.39E-9	10.76	7.3E-27	0.035	0.027
AD-Young vs. WT-Young	0.110	0.012	8.183	6.1E-17	1.50E-3	1.000
WT-Old vs. WT-Young	0.379	1.1E-14	18.94	6.7E-64	0.037	0.036

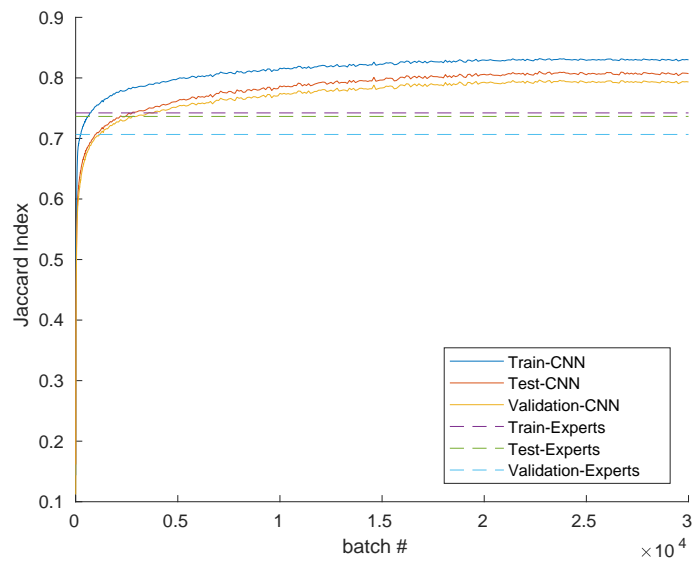


Figure S1: Jaccard as a measure of the model accuracy. The *DeepVess* results surpass expertsthe human annotator result at all three train, validation, and test datasets. The expert and CNNhuman annotator and *DeepVess* results are show in dashed and solid lines respectively. The differences between three datasets results for both *DeepVess* and expertshuman annotator are due variability of the MPM image qualities. The constant difference between *DeepVess* and experts'human annotator's result confirm the avoidance of overfitting.

Table S2: The results of investigating different field of view sizes.

	<i>Architecture</i>	<i>FOV</i>
N1	C 7x7x5 - P - C 5x5 - P - NN	33x33x5
N2	C 7x7x9 - P - C 5x5 - P - NN	33x33x9
N3	C 7x7x15 - P - C 5x5 - P - NN	33x33x15
N4	C 7x7x31 - P - C 5x5 - P - NN	33x33x31
N5	C 7x7x5 - P - C 5x5 - P - NN	85x85x5
N6	C 7x7x7 - P - C 5x5 - P - NN	25x25x7
N7	C 7x7x7 - P - C 5x5 - P - NN	33x33x7
N8	C 7x7x7 - P - C 5x5 - P - NN	41x41x7
N9	C 9x9x9 - P - C 5x5 - P - NN	41x41x9

	<i>Sensitivity</i>	<i>Specificity</i>	<i>Precision</i>	<i>Dice</i>	<i>Jaccard</i>	<i>MHD</i>
N1	93.10%	98.15%	81.84%	87.11%	77.17%	1.38
N2	87.39%	98.87%	87.41%	87.40%	77.62%	1.15
N3	91.69%	98.31%	82.93%	87.09%	77.13%	1.61
N4	89.94%	98.21%	81.82%	85.69%	74.96%	2.19
N5	91.15%	98.23%	82.18%	86.43%	76.11%	1.46
N6	90.22%	98.61%	85.34%	87.71%	78.11%	1.03
N7	91.57%	98.49%	84.49%	87.89%	78.40%	1.20
N8	91.01%	98.34%	83.07%	86.86%	76.77%	1.85
N9	93.23%	97.61%	77.80%	84.81%	73.63%	2.38

Table S3: The results of investigating different architectures.

	<i>Architecture</i>	<i>FOV</i>
N10	C 7x7x7 - P - C 5x5 - P - 2*NN	33x33x7
N11	3*C 3x3x3 - P - 3*C 3x3 - P - NN	33x33x7=
N12	4*C 5x5x5 - P - 3*C 5x5 - P - NN	41x41x9
N13	4*C 3x3x3 - P - 3*C 3x3 - P - NN	41x41x9
N14	C 7x7x7 - P - C 5x5x5 - P - NN	25x25x25
N15	3*C 3x3x3 - P - 2*C 3x3x3 - P - NN	33x33x33
N16	3*C 3x3x3 - P - 2*C 3x3 - P - NN	41x41x41
N17	3*C 3x3x3 - P - 2*C 3x3 - P - NN	31x31x31
N18	3*C 3x3x3 - P - 2*C 3x3 - P - NN	49x49x49
N19	3*C 3x3x3 - P - 2*C 3x3 - P - NN	33x33x7
N20	previous architecture for ROI 5x5	33x33x7
N20P	previous architecture+post proc.	33x33x7

	<i>Sensitivity</i>	<i>Specificity</i>	<i>Precision</i>	<i>Dice</i>	<i>Jaccard</i>	<i>MHD</i>
N10	89.61%	98.33%	82.78%	86.06%	75.53%	1.63
N11	93.71%	97.83%	79.46%	86.00%	75.44%	1.87
N12	83.78%	98.68%	85.09%	84.43%	73.05%	1.82
N13	93.45%	98.15%	81.90%	87.30%	77.46%	1.48
N14	91.57%	98.49%	84.49%	87.89%	78.40%	1.20
N15	90.29%	98.40%	83.51%	86.77%	76.63%	5.98
N16	6.31%	93.76%	8.31%	7.17%	3.72%	9.45
N17	14.82%	85.51%	8.39%	10.71%	5.66%	9.48
N18	30.40%	72.32%	8.96%	13.85%	7.44%	9.50
N19	92.89%	98.31%	83.12%	87.74%	78.15%	1.16
N20	95.15%	98.40%	84.18%	89.33%	80.71%	1.58
N20P	95.09%	98.47%	84.80%	89.65%	81.24%	1.04